Calibration of the Circle-plus-Arc Trajectory

Stefan Hoppe, *Student Member, IEEE,* Frédéric Noo, *Member, IEEE,* Frank Dennerlein, *Student Member, IEEE,* Günter Lauritsch, and Joachim Hornegger

***Abstract*— In this paper, a novel calibration method for C-arm cone-beam (CB) scanners is presented which allows the calibration of the circle-plus-arc trajectory. The circle-plus-arc trajectory has been investigated recently for exact image reconstruction and is especially well suited for C-arm systems. The main idea is the separation of the trajectory into two segments (circle segment and arc segment) which are calibrated independently. For each trajectory segment, a calibration phantom is placed in an optimal way. The calibration results are then combined by computing the transformation the phantom experienced in-between the independent runs. This combination can be done in a postprocessing step by using the Singular Value Decomposition (SVD). The method works for any calibration procedure in which the phantom has a favored orientation with respect to a trajectory segment. Results are presented for both, simulated as well as real data acquired with a Siemens AXIOM Artis C-arm system.**

I. Introduction

Due to their open design, C-arm systems unlike computed tomography (CT) systems are not capable of acquiring projections along an ideal trajectory [1]. These deviations have to be determined by a calibration procedure prior to image reconstruction in order to avoid severe reconstruction artifacts [2], [3]. Fortunately, from scan to scan, the C-arm deviates almost in the same way from the ideal trajectory, so that the calibration can be done off-line with updating only needed about once per year in clinical environments. The term calibration here refers to the estimation of all parameters which completely describe the geometry of the CB data acquisition system (Section II-A). Various calibration methods have been suggested in the literature (e.g. [1], [2], [4]). For C-arm CT, the high-resolution requirements demand a robust calibration method. Such a method was suggested in [1] for a circular trajectory and has been successfully applied to calibrate numerous routinely-used C-arm systems.

This work presents a calibration procedure for the circle-plus-arc trajectory that builds on the robustness of the method in [1]. This work is motivated by the recent development of exact reconstruction algorithms for a circle-plus-arc data acquisition [5], [6]. Our main idea for calibration is the separation of the trajectory into two segments (circle segment and arc segment) which are calibrated independently. From there we proceed in two major steps: (i) independent calibration of the circle and the arc segment where for each calibration run, a calibration object is placed optimally with respect to the segment under consideration (Section II-B, II-C) and (ii) combination of the calibration results by computing the transformation the phantom experienced in-between the independent runs (Section III). After a brief review of the calibration problem for a circular trajectory in Section II, the details of our calibration procedure are exposed in Section III. Experimental results are given in Section IV.

S. Hoppe and J. Hornegger are with the Institute of Pattern Recognition (LME), University of Erlangen-Nuremberg, Erlangen, Germany.

F. Noo and F. Dennerlein are with the Department of Radiology (UCAIR), University of Utah, Salt Lake City, UT, USA.

G. Lauritsch is with the Siemens AG, Medical Solutions, Forchheim, Germany.

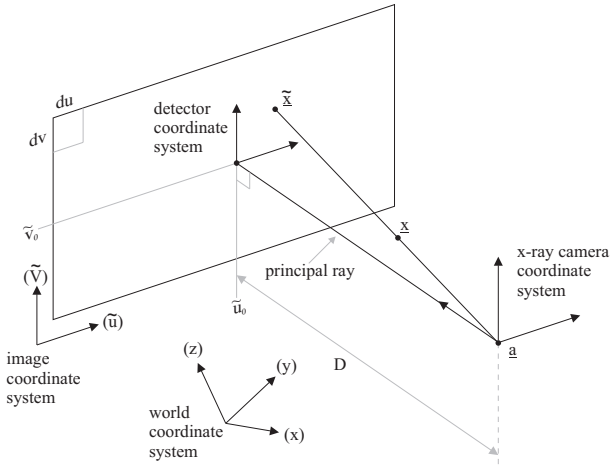

Fig. 1. A projection matrix describes a mapping of a point $\underline{x}$ from 3D world coordinates to 2D image coordinates $\underline{\tilde{x}}$ and thus contains all geometrical information about the C-arm device for a given CB projection.

II. Background

A. Scanner Geometry

In C-arm CT, the scanner geometry is usually described by assigning to each measurement position one projection matrix P that includes all geometrical information about the measurement. Using homogeneous coordinates, P appears as a matrix of size 3×4 that maps any point $\underline{x}$ expressed in the 3D world coordinate system to a point $\underline{\tilde{x}}$ expressed in the 2D detector coordinate system according to the formula

$$\underline{\tilde{x}} = P\underline{x}. \tag{1}$$

This mapping can be decomposed in three successive steps, see Figure 1: (i) transformation of the point from world coordinates to x-ray camera coordinates (Euclidian transformation), (ii) projection of the point onto the detector plane where it is represented by detector coordinates (central projection), (iii)

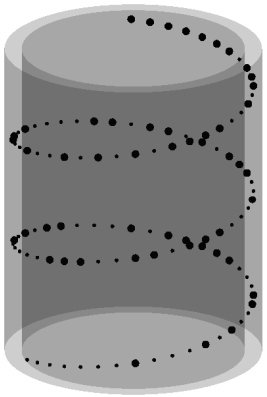

Fig. 2. The calibration phantom contains 108 steel spheres. The big spheres constitute a logical one and the small spheres constitute a logical zero.

transformation of the point to image (pixel) coordinates (affine transformation):

$$P = \underbrace{\begin{bmatrix} \frac{1}{du} & s & \tilde{u}_0 \\ 0 & \frac{1}{dv} & \tilde{v}_0 \\ 0 & 0 & 1 \end{bmatrix}}_{\text{affine transformation}} \underbrace{\begin{bmatrix} D & 0 & 0 & 0 \\ 0 & D & 0 & 0 \\ 0 & 0 & 1 & 0 \end{bmatrix}}_{\text{central projection}} \underbrace{\begin{bmatrix} R & -R\underline{a} \\ \underline{0}^T & 1 \end{bmatrix}}_{\text{Euclidian transformation}} . \tag{2}$$

In this decomposition, R is a 3×3 rotation matrix giving the detector orientation, $\underline{a}$ is a 3×1 vector describing the x-ray source position in the world coordinate system [7], D is the focus-to-detector distance, du is the pixel width, dv is the pixel height, and s is known as the "skew" parameter because a value of s other than zero amounts to a device with a sheared detector pixel grid. Also, $(\tilde{u}_0, \tilde{v}_0)^T$ are the coordinates of the orthogonal projection of the source position onto the detector plane. These coordinates are in the image coordinate system, the origin $(0, 0)^T$ of which is at the lower left corner of the image.

B. Calibration Phantom

A CB projection of the calibration phantom at a given source-detector position typically allows the determination of the projection matrix P for this position (see also Section II-C). The geometrical shape of the calibration phantom is exactly known in the world coordinate system. The world coordinate system is attached to the phantom. Often, the phantom consists of various spheres of high attenuation that are distributed over a control region of predefined extent and that are enclosed in low attenuation base material. In this work, we use a spiral phantom. This phantom was originally designed to calibrate a trajectory consisting of a circle or partial circle for subsequent Feldkamp reconstruction. It consists of a cylindrical wall made of plastics which has almost no x-ray attenuation. Its outer radius is 72 mm and its inner radius is 62 mm measured from the axis of rotation. The height of the cylinder is 205.8 mm. Inside the wall, there are 108 spheres made of noncorrosive steel with two different radii arranged along a spiral-shaped path. The large spheres have a diameter of 3.6 mm and the small spheres have a diameter of 1.6 mm. The sequence of alternating large and small spheres represents a binary string with an 8 bit encoding, such that an arbitrary subsequence of length 8 provides enough information to identify each sphere of the sequence uniquely within the whole binary string. This encoding is used to establish unique correspondences between the projection of the spheres in the image and their 3D counterparts. A sketch of this phantom is shown in Figure 2.

C. Calibration Algorithm

To calibrate a circular short-scan or full-scan trajectory, the (spiral) phantom is placed near the iso-center of the scan with its main symmetry axis (almost) parallel to the rotation axis. This arrangement guarantees that most spheres are visible during the scan with only minor overlaps in regions where the projection of the spiral exhibits high curvature. The calibration procedure consists of four major steps: (i) localization of the spheres in the image, (ii) ordering of the located spheres, (iii) establishment of unique correspondence between the projection of the spheres in the images and their 3D counterparts by decoding binary substrings of length 8, and (iv) estimation of the projection matrix for each source position. The last step is described in more details in [1]. Once an initial estimate of the projection matrix is available, additional spheres can be located in the image by projecting all spheres in the image plane using the estimated projection matrix, and performing then a neighbor search around the projection of previously unlocated spheres. The process is repeated until a prescribed percentage of all spheres has been found.

III. Calibration of the Circle-plus-Arc Trajectory

The spiral phantom is well suited to calibrate each segment of a circle-plus-arc trajectory. However, to do so the phantom needs to be positioned differently for each segment, so that the projections of the spheres are arranged along an "S-curve" in every CB image acquired along that segment. Otherwise, when the phantom is observed from oblique viewing directions, spheres may overlap in the projection and the projected spiral may cross over itself, so that the task of locating and ordering the spheres becomes impossible. Indeed, for the circle-plus-arc trajectory, only the first $11°$ or so of the arc segment can be reliably calibrated with the phantom in the position associated to the circular scan (see Figure 3a). However, the arc length required to obtain complete data for reconstruction is typically of $22°$.

When placing the phantom differently from one segment of the trajectory to the other (Figure 3), one encounters the problem that the projection matrices obtained for the segments refer to different coordinate systems and have to be registered such that they refer to a common coordinate system. We have developed a method to achieve this registration, providing thereby a way to calibrate the circle-plus-arc trajectory as a whole, using optimal placement of the phantom for each of its segments. The registration was done through the determination of the change in position and orientation applied to the phantom

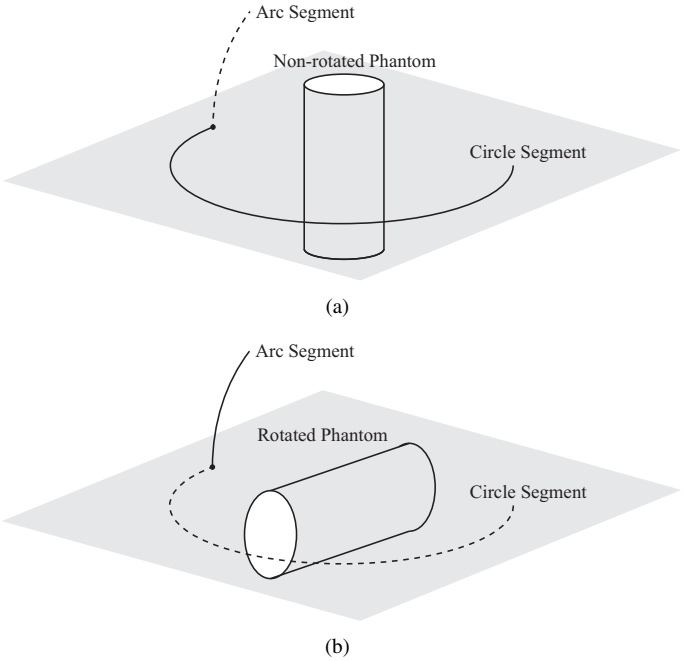

Fig. 3. The calibration setup for the circle-plus-arc trajectory for (a) the circle and (b) the arc segment is shown. Here, the phantom placement to calibrate the arc segment differs from that of the circle segment by a 90 degree rotation.

from calibration of the first segment to the next one, using information provided by so called "connection points" (CPs). The term connection point refers to any source position for which two projection matrices can be obtained – one using the non-rotated phantom and the other one using the rotated phantom. Assume we have determined the projection matrices P and P' of such a CP (e.g. located on the arc segment) by applying the calibration procedure of Section II-C. We set out then the goal of finding the 4×4 matrix H that maps P' onto P as follows:

$$P = P'H. \tag{3}$$

This matrix H can as well be used to transform all other projection matrices. In order to compute H, we make use of the connection between a set of known 3D points $\underline{x}_i$ and their 2D images $\underline{\tilde{x}}_i$ related by P

$$\underline{\tilde{x}}_i = P\underline{x}_i. \tag{4}$$

In this system of equations, all quantities are known. To incorporate the unknown matrix H, relation (3) can be used to replace P by $P'H$. This gives

$$\underline{\tilde{x}}_i = P'H\underline{x}_i, \tag{5}$$

which has to be solved for H. By writing the unknown entries of H row-wise into a 16×1 vector $\underline{h}$, we can reformulate (5) to a linear equation of $\underline{h}$, such that after some calculation (see Appendix I for details), the following system of equations is generated

$$A_i\underline{h} = \underline{0}, \tag{6}$$

	Simulated CB data	Real CB data
Radius (R) [mm]	750	750
Focal length (D) [mm]	1200	1200
Pixel width (du) [mm/px]	0.372	0.372
Pixel height (dv) [mm/px]	0.372	0.372
Detector dimension [px^2]	1024 $\times$ 1024	1024 $\times$ 1024
Angular sampling (circle) [°/projection]	0.4	0.4
Angular sampling (arc) [°/projection]	0.4	0.4
Number of projections (circle scan)	538 (214.8°)	538 (214.8°)
Number of projections (arc scan)	50 (19.6°)	50 (19.6°)
Number of valid CPs (arc scan)	28 (10.8°)	31 (12.0°)

TABLE I

where the measurement matrix A_i consists only of known quantities $\underline{\tilde{x}}_i, \underline{x}_i, P'$ and is of dimension 2×16 because each tupel $(\underline{\tilde{x}}_i; \underline{x}_i)$ provides two linearly independent equations. Therefore, a theoretical minimum of at least $N = 8$ A_i's are required to determine all 16 entries of $\underline{h}$. By stacking all A_i's on top of each other, a matrix B of dimension $2N \times 16$ can be generated with

$$B\underline{h} = \underline{0}, \tag{7}$$

where

$$B = \begin{bmatrix} A_1 \\ A_2 \\ \vdots \\ A_N \end{bmatrix}, \tag{8}$$

and $N \geq 8$.

A linear solution for $\underline{h}$ to this over-determined system of equations is provided by the singular vector corresponding to the smallest singular value of B by using the SVD (see [7]). In general, the points $\underline{\tilde{x}}_i$ may be chosen arbitrarily as long as they are well distributed inside the field of view (see also [1]). Practically, these points can be generated from equation (4), with the $\underline{x}_i$'s being the midpoints of the spheres of the calibration phantom. This gives a matrix B with N=108.

It is a simple matter to extend this procedure to more than one CP to improve accuracy. From each connection point CP_k, with $k = 1 \ldots K$, a $2N \times 16$ measurement matrix B_k is obtained. Again, the B_k's can be stacked on top of each other resulting in a matrix C of size $2NK \times 16$. The system is solved by finding the right null-vector of C using the SVD as before.

IV. Experiments

Experiments were performed using simulated as well as real CB data acquired with a AXIOM Artis dBA C-arm system (Siemens AG, Medical Solutions, Forchheim, Germany). For the simulation, a detailed computer model of the calibration phantom was created. The corresponding CB projections were generated using an analytical forward projector. The phantom was rotated by 90° according to Figure 3b but in addition translated by 10 mm along the z-axis to mimic a realistic phantom motion. The parameters of the experiments are given in Table I. In Figure 4, the root mean square (RMS) error between the true and registered projection matrices P and

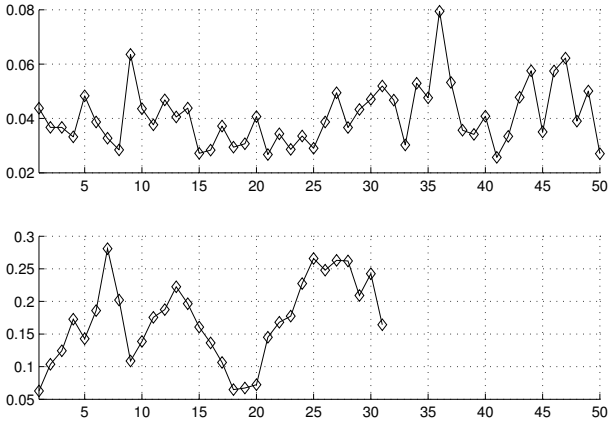

Fig. 4. Calibration accuracy from simulated (top) and real CB data (bottom) for the calibrated arc segment. In each case, the projection number is plotted against the RMS error given in pixel units. Projection 50 corresponds to the last source position (at 19.6°) along the arc segment.

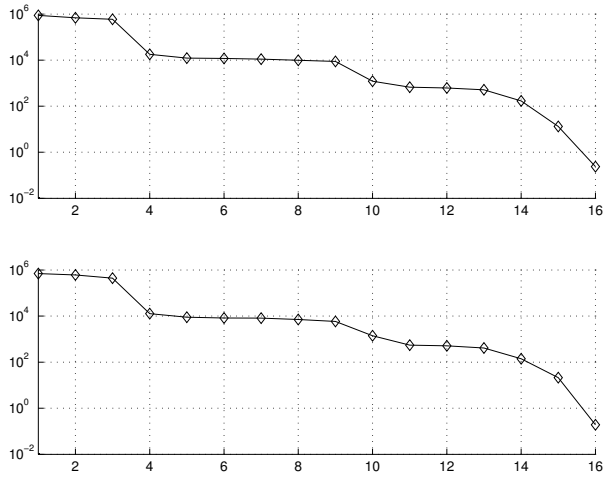

Fig. 5. Singular values $s_1 \dots s_{16}$ of the composed measurement matrix C for simulated (top) and real CB data (bottom). In each case, the singular values are plotted in descending order using a logarithmic scale.

$P^{(r)}$ of the arc segment is shown for the simulated and the real experiment. The RMS error was computed from image measurements using

$$\sigma^{(RMS)} = \left(\frac{1}{N} \sum_{i=1}^{N} \left(\tilde{\underline{x}}_i - \tilde{\underline{x}}_i^{(r)} \right)^2 \right)^{1/2}, \qquad (9)$$

with $N = 108$, where $\tilde{\underline{x}}_i = P\underline{x}_i$ and $\tilde{\underline{x}}_i^{(r)} = P^{(r)}\underline{x}_i$ denote the true and estimated image points respectively (after the homogenous scaling factor has been removed) of the midpoints $\underline{x}_i$ of the steel spheres of the calibration phantom. For the real experiment, 31 projection matrices could be calibrated from the non-rotated phantom and were used as the ground truth. Every second projection matrix thereof was also used for the registration to compute the matrix H.

The RMS error gives an estimate of how much the average projected point deviates from its true position. A different error measurement may be chosen instead. For example, Faugeras [8] suggests a decomposition of the projection matrices to obtain every calibration parameter e.g. x-ray source position, focus-to-detector distance, skew etc. However, by comparing these values separately, we get only little insight into how accurately the point mapping itself behaves, because deviations from different such measurements may cancel each other when acting together on a point in 3-space. For this reason, we suggest to measure the error from image measurements instead.

From the figure it is observed that our approach achieves sub-pixel accuracy even with real data. The accuracy of real data is reduced by a factor of 5 compared to ideal data because of higher errors in the underlying calibration procedure (sphere localization etc.) and because the ground truth is only known approximately. To get an impression of the achieved accuracy, Figure 6 and Figure 7 show the projection of the midpoints of the steel spheres of the calibration phantom onto the acquired projection images for simulated and real CB data, respectively. In Figure 6a and 7a, the points were projected with the projection matrices which are associated to the minimal RMS error, while in Figure 6b and 7b, the projection matrices which are associated to the maximal RMS error were used. The figures confirm the high accuracy of our method.

Figure 5 shows the singular values $s_1 \dots s_{16}$ of the composed measurement matrix C with dimension $2NK \times 16$ for the simulated ($N = 108, K = 28$) and the real ($N = 108, K = 16$) experiment. A few observations: (i) The plots for simulated and real data are almost identical. (ii) The smallest singular value s_{16} is close to zero. (iii) Singular Value s_{16} differs from s_{15} by a factor of magnitude 10^2, while any other two successors differ by a factor of magnitude 10 or less. (iv) The difference between s_1 and s_{16} is in the order of 10^7. From (i), we see that the simulated and the real data set have the same numerical characteristics. Thus, with our simulation, the numerical behaviour of a real system is reproducible. From (ii), (iii) and (iv), we conclude that the system is numerically stable and that the matrix C has a one-dimensional null-space as required. The fact that s_{16} is close to but not exactly equal to zero, can be blamed on measurement errors (e.g. from the sphere localization of the underlying calibration procedure).

Figure 8 shows one slice of a human head phantom, which was reconstructed using the M-line approach according to [9]. The CB data was again acquired with the AXIOM Artis *d*BA C-arm system (Siemens AG, Medical Solutions, Forchheim, Germany). Therefore, the setup is the same as in Table I. For the calibration of the system, all 31 CPs were used to compute the matrix H. The reconstruction shows a perfect geometry and even small details can be clearly distinguished.

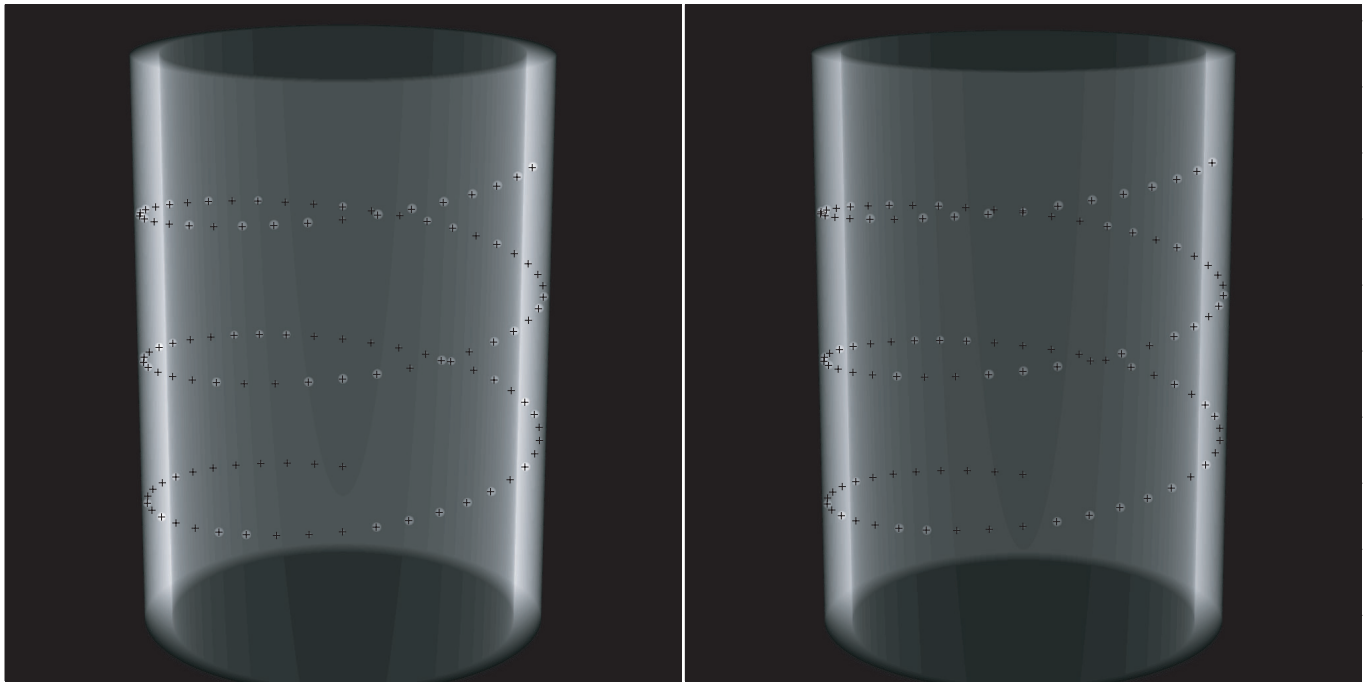

(a) (b)

Fig. 6. Projection of the midpoints of the steel spheres of the calibration phantom onto the simulated CB data associated with (a) the minimal (projection 41) and (b) the maximal (projection 36) RMS error.

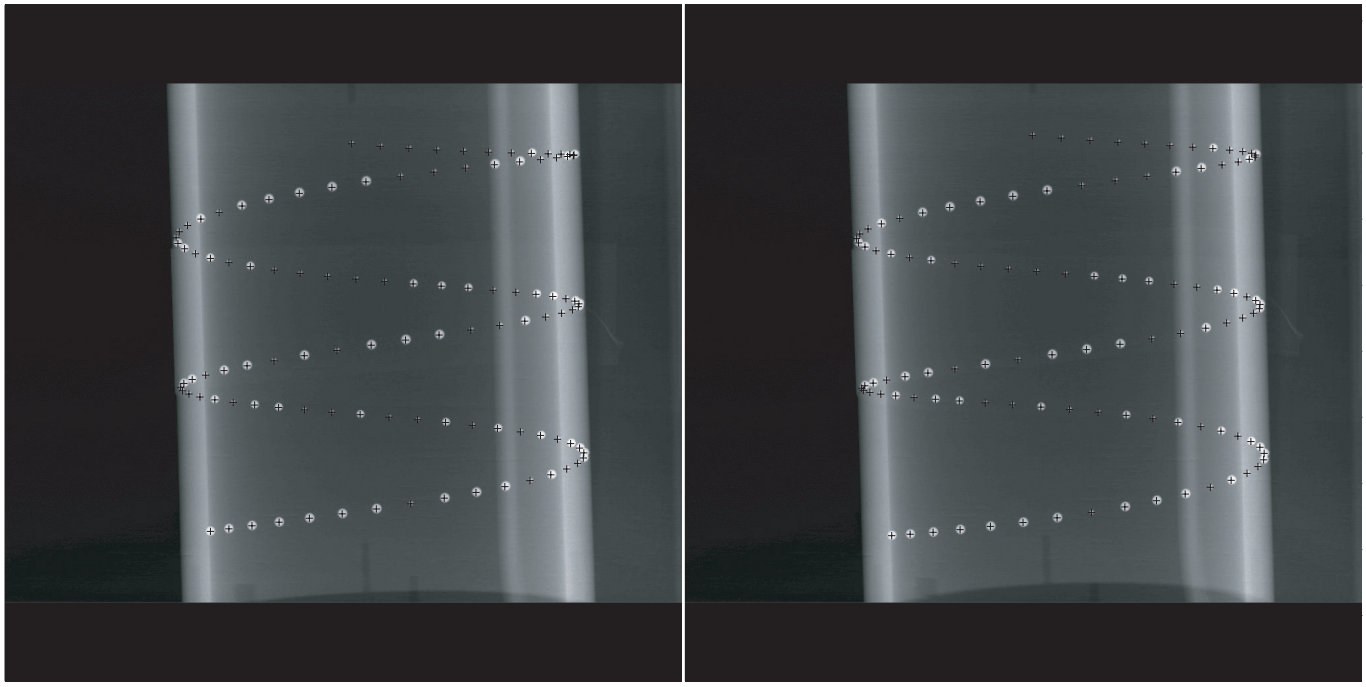

(a) (b)

Fig. 7. Projection of the midpoints of the steel spheres of the calibration phantom onto the real CB data associated with (a) the minimal (projection 1) and (b) the maximal (projection 7) RMS error.

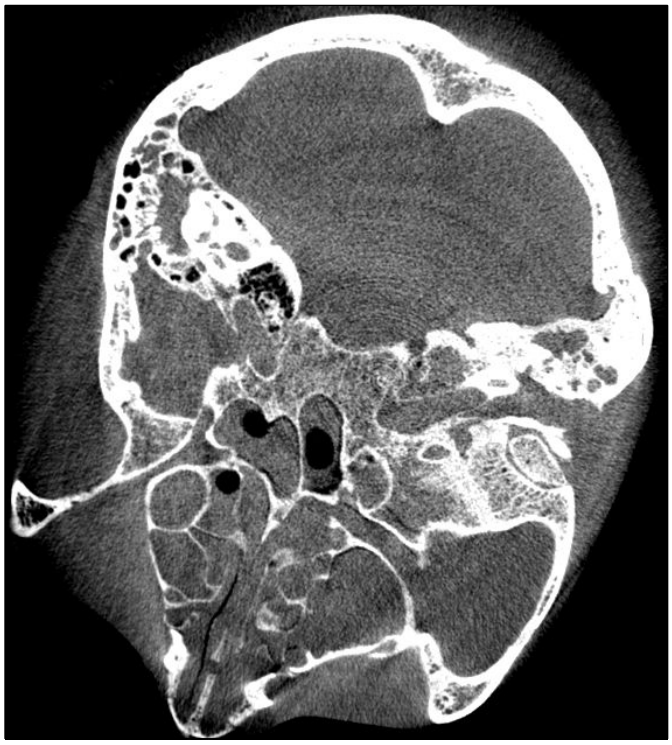

Fig. 8. Reconstruction of a human head phantom from real CB data. The slice is 53 mm away from the plane of the circular scan. The window was set to C=0 HU, W=1000 HU.

V. Conclusions

We have presented a method to calibrate the circle-plus-arc trajectory. The idea of combining different trajectory segments by identifying the phantom transformation applies to any calibration procedure in which the phantom has a favored orientation with respect to a trajectory segment. Experiments for simulated and real data show that the method works with sub-pixel accuracy. Our calibration results have also been confirmed with a reconstruction of a human head phantom using real CB data.

Appendix I
Determination of the Measurement Matrix

In this appendix, we show how the entries of the measurement matrix A_i can be determined (see also [7]). Our starting point is equation (5)

$$\tilde{\underline{x}}_i = P' H \underline{x}_i.$$

We proceed by applying the vector cross product to get

$$\tilde{\underline{x}}_i \times P' H \underline{x}_i = \underline{0}.$$

We denote the j–th row of the matrix P' by $\underline{p}'^{jT}$ and the j–th column of the matrix H by $\underline{h}_j$ and also $\underline{x}_i = (x_i, y_i, z_i, 1)^T$. As an intermediate result, we find

$$P' H \underline{x}_i = \begin{pmatrix} x_i \underline{p}'^{1T} \underline{h}_1 + y_i \underline{p}'^{1T} \underline{h}_2 + z_i \underline{p}'^{1T} \underline{h}_3 + \underline{p}'^{1T} \underline{h}_4 \\ x_i \underline{p}'^{2T} \underline{h}_1 + y_i \underline{p}'^{2T} \underline{h}_2 + z_i \underline{p}'^{2T} \underline{h}_3 + \underline{p}'^{2T} \underline{h}_4 \\ x_i \underline{p}'^{3T} \underline{h}_1 + y_i \underline{p}'^{3T} \underline{h}_2 + z_i \underline{p}'^{3T} \underline{h}_3 + \underline{p}'^{3T} \underline{h}_4 \end{pmatrix}.$$

By setting $\tilde{\underline{x}}_i = (\tilde{x}_i, \tilde{y}_i, \tilde{w}_i)$, the cross product can be written as

$$\tilde{\underline{x}}_i \times P' H \underline{x}_i = \begin{pmatrix} a x_i \underline{h}_1 + a y_i \underline{h}_2 + a z_i \underline{h}_3 + a \underline{h}_4 \\ b x_i \underline{h}_1 + b y_i \underline{h}_2 + b z_i \underline{h}_3 + b \underline{h}_4 \\ c x_i \underline{h}_1 + c y_i \underline{h}_2 + c z_i \underline{h}_3 + c \underline{h}_4 \end{pmatrix} = \underline{0},$$

with

$$a = \tilde{y}_i \underline{p}'^{3T} - \tilde{w}_i \underline{p}'^{2T} \quad b = \tilde{w}_i \underline{p}'^{1T} - \tilde{x}_i \underline{p}'^{3T} \quad c = \tilde{x}_i \underline{p}'^{2T} - \tilde{y}_i \underline{p}'^{1T}.$$

Equivalently,

$$\tilde{\underline{x}}_i \times P' H \underline{x}_i = \begin{bmatrix} a x_i & a y_i & a z_i & a \\ b x_i & b y_i & b z_i & b \\ c x_i & c y_i & c z_i & c \end{bmatrix} \begin{pmatrix} \underline{h}_1 \\ \underline{h}_2 \\ \underline{h}_3 \\ \underline{h}_4 \end{pmatrix} = \underline{0}.$$

Because only two equations are linearly independent, the third one can be omitted. Thus, we chose

$$A_i = \begin{bmatrix} a x_i & a y_i & a z_i & a \\ b x_i & b y_i & b z_i & b \end{bmatrix},$$

with a and b as defined above.

Acknowledgments

This work was supported by Siemens AG, Medical Solutions and was supported in part by the U.S. National Institutes of Health (NIH) under grant R01 EB000627.

References

[1] N. K. Strobel, B. Heigl, T. M. Brunner, O. Schuetz, M. M. Mitschke, K. Wiesent, and T. Mertelmeier. Improving 3D image quality of x-ray C-arm imaging systems by using properly designed pose determination systems for calibrating the projection geometry. *Proc. of SPIE*, 5030:943–954, 2003.

[2] F. Noo, R. Clackdoyle, C. Mennessier, T.A. White, and T.J. Roney. Analytic method based on identification of ellipse parameters for scanner calibration in cone-beam tomography. *Physics in Medicine and Biology*, 45(11):3489–3508, 2000.

[3] K. Wiesent, K. Barth, N. Navab, P. Durlak, T. Brunner, O. Schuetz, and W. Seissler. Enhanced 3-d-reconstruction algorithm for c-arm systems suitable for interventional procedures. *IEEE Transactions on Medical Imaging*, 19(5):391–403, 2000.

[4] D. Beque, J. Nuyts, P. Suetens, and G. Bormans. Optimization of geometrical calibration in pinhole spect. *IEEE Transactions on Medical Imaging*, 24(2):180–190, 2005.

[5] A. Katsevich. Image reconstruction for the circle-and-arc trajectory. *Physics in Medicine and Biology*, 50(10):2249–2265, 2005.

[6] J. Pack and F. Noo. Cone-beam reconstruction using 1d filtering along the projection of m-lines. *Inverse Problems*, 21(3):1105–1120, 2005.

[7] R. Hartley and A. Zisserman. *Multiple View Geometry in Computer Vision*. Cambridge University Press, 2nd edition, 2003.

[8] O. Faugeras. *Three-Dimensional Computer Vision: A Geometric Viewpoint*. MIT Press, 2nd edition, 1996.

[9] S. Hoppe, F. Dennerlein, G. Lauritsch, J. Hornegger, and F. Noo. Cone-beam tomography from short-scan circle-plus-arc data measured on a c-arm system. In *IEEE Medical Imaging Conference*, San Diego, CA, USA, Oct. 29 - Nov. 4, 2006 (to appear).